Journal of Metals, Materials and Minerals, 36(1), e2309, 2026

Synthesis, structure, and electrochemical properties of the $Ni(OH)_2/NiMoO_4$ composite on the rGO/NF template for hybrid battery-supercapacitor electrodes

Retno ASIH[1,*], Haniffudin NURDIANSAH[2], Rogabe SIANIPAR[2], Ida Ayu GAYATRI[2], Lukman NOEROCHIM[2], Diah SUSANTI[2], Isao WATANABE[3], and Darminto DARMINTO[1]

[1] *Department of Physics, Institut Teknologi Sepuluh Nopember, Surabaya, 60111, Indonesia*
[2] *Department of Material and Metallurgical Engineering, Institut Teknologi Sepuluh Nopember, Surabaya, 60111, Indonesia*
[3] *Nuclear Structure Research Group, RIKEN Nishina Center, 2-1 Hirosawa, Wako, Saitama, 351-0198, Japan*

***Corresponding author e-mail**: retno.asih@its.ac.id

Received date:
12 February 2025
Revised date:
16 July 2025
Accepted date:
22 October 2025

Keywords:
Electrochemical performance;
Electrodes;
Hybrid battery-supercapacitor;
$Ni(OH)_2/NiMoO_4$/rGO/NF

Abstract

The growing demand for renewable and sustainable energy has intensified research on advanced energy-storage systems that can deliver both high energy and power densities. In this study, a $Ni(OH)_2/NiMoO_4$ composite on a reduced graphene oxide/nickel foam (rGO/NF) template was synthesized through a hydrothermal and electrodeposition route to construct a hybrid battery-supercapacitor electrode. The unique hierarchical design combines the pseudocapacitive activity of $Ni(OH)_2/NiMoO_4$ with the excellent conductivity of rGO and the high surface area of NF, enabling efficient electron and ion transport. Structural and morphological analyses confirm the successful formation of the $Ni(OH)_2/NiMoO_4$/rGO/NF architecture. The electrode exhibits a specific capacitance (C_s) of ~358 $F\cdot g^{-1}$ at 5 $mV\cdot s^{-1}$, an energy density of ~24 $Wh\cdot kg^{-1}$, a power density of ~626 $W\cdot kg^{-1}$, a conductivity of 1.30 $S\cdot m^{-1}$ (0.01 kHz), and retains ~86% capacitance after 50 cycles. These findings demonstrate that the synergistic integration of multiredox $Ni(OH)_2/NiMoO_4$ with conductive rGO/NF enhances electrochemical performance, providing effective design strategy for developing hybrid battery-supercapacitor electrodes.

1. Introduction

Global energy consumption remains heavily dependent on fossil fuels, which accounted for 83% of total global energy use in 2023 [1]. Continued reliance on these resources accelerates environmental degradation and could increase global temperatures by ~3°C by the end of this century. To limit warning, carbon dioxide (CO_2) emissions must reach net zero by 2050 [2]. Moreover, fossil fuel reserves are finite, driving the need for sustainable energy technologies, including efficient energy storage systems [3].

Batteries, the dominant energy storage technology, offer high energy density at relatively low cost but suffer from low power density, limited lifespan, and performance degradation under high charge/discharge rates [4]. Supercapacitors, in contrast, deliver high power density, long cycle life, rapid charge/discharge, and low maintenance [5], but have lower energy density than batteries. Integrating both into a hybrid energy storage system can combine their advantages: in electric vehicles (EVs), for instance, the battery supplies long-range energy, while the supercapacitor buffers power surges during acceleration or braking, extending battery life and reducing degradation [4].

One promising effort to improve the performance of hybrid battery-supercapacitors is by using $Ni(OH)_2/NiMoO_4$ composites on a rGO/NF template. rGO is a graphene derivative with similar features as that of graphene to some extent and has the remaining oxygen functionalities [6,7]. rGO is commonly prepared from graphite which undergoes an oxidation process followed by reduction in which some of the oxygen groups are removed, making rGO easily react with other materials [8,9]. rGO exhibits high electrical capacitance and surface area; therefore, it has potentially been used as an electrode material in batteries and supercapacitors. rGO stores charge predominantly via the electrostatic accumulation of ions at the electrode-electrolyte interface, a non-Faradaic process typical of electric double-layer capacitors (EDLCs) and symmetric charge storage systems. Its ability to store high energy is required in hybrid battery-supercapacitor systems [10].

Nickel-rich cathodes have emerged as a promising alternative in battery technology, offering structural stability and high operating potential for enhanced electrochemical performance [11]. $Ni(OH)_2$, a typical pseudocapacitive or battery-type material, stores charge primarily through Faradaic redox reactions between $Ni(OH)_2$ and NiOOH in alkaline electrolytes and has been widely applied in asymmetric supercapacitor [12]. While the synthesis of $Ni(OH)_2$ nanosheets on $NiMoO_4$ nanorods has been reported [13], their integration with a symmetric EDLC-type material such as rGO remains unexplored. $NiMoO_4$, a molybdate-based material, provides high capacitance, low cost, abundant resources, and environmental friendliness but suffers from limited rate capability and cycle life [14,15]. Therefore, combining $NiMoO_4$ with $Ni(OH)_2$ in a composite structure offers a promising strategy to enhance the overall performance of hybrid electrodes.

As a template, nickel-based substrates such as NF and nickel-conducting cloth serve as electrode supports due to their high density and large surface area [16]. NF can increase the bond between the active materials and facilitate efficient charge transfer [17]. In this study,

DOI:10.55713/jmmm.v36i1.2309

hydrothermal and electrodeposition methods are used to achieve the desired hierarchical structure on the electrode.

The novelty of this work lies in the strategic integration of $Ni(OH)_2$/$NiMoO_4$ composites with rGO on an NF template to form a hierarchical hybrid electrode structure. While $Ni(OH)_2$/$NiMoO_4$ composites have previously been explored in asymmetric supercapacitors [13], achieving a capacitance of 121 F·g^{-1} at 10 A·g^{-1} with 77% retention after 5000, their coupling with a symmetric charge storage component such as rGO within a single electrode architecture has not been reported. This design simultaneously combines (i) the multiple redox-active sites of $Ni(OH)_2$ and $NiMoO_4$ for enhanced pseudocapacitance, (ii) the high electrical conductivity and surface area of rGO for rapid charge transport, and (iii) the mechanical robustness and high surface area of NF for strong adhesion and efficient ion/electron pathways. This synergistic configuration results in improved specific capacitance, energy density, conductivity, and discharge time, making the electrode a promising candidate for next-generation hybrid battery-supercapacitor devices.

2. Experimental

2.1 Materials synthesis

The synthesis process is carried out in four stages, as illustrated in Figure 1. rGO was prepared from graphite (Dingshengxin ISO9001) by a modified Tour route. Details of the route can be found elsewhere [18]. The obtained rGO was then coated on NF to form the rGO/NF template. $NiMoO_4$ was fabricated by a hydrothermal method on the rGO/NF template inside an autoclave. Lastly, $Ni(OH)_2$ was prepared by electrodeposition process of $Ni(NO_3)_2.6H_2O$ onto $NiMoO_4$/rGO/NF.

2.1.1 Preparation of the rGO/NF template

NF with a size of 5 cm × 6 cm was cleaned ultrasonically with acetone, 3 M hydrochloric acid (HCl, 37%, SAP chemicals), deionized (DI) water, and ethanol alternately for 10 min. Then, 10 mg of the prepared rGO was added to 30 mL of distilled water and then ultrasonicated for 90 min. 30 mg of ascorbic acid ($C_6H_8O_6$, Merck) was dispersed into the rGO solution and stirred for 10 min at room temperature to obtain an rGO suspension. The cleaned NF was soaked in the suspension and then heated in a water bath at 90°C for 6 h. The rGO/NF was cleaned with DI water and ethanol (C_2H_6O 70%, SAP chemicals) to reach neutral pH and then dried in a vacuum at 60°C for 2 h.

2.1.2 Hydrothermal route for the synthesis of $NiMoO_4$ on the rGO/NF template

The process of making $NiMoO_4$/rGO/NF begins by adding 40 mL of 0.1 M $Na_2MoO_4.2H_2O$ (99.5%, Himedia PCT0117) into 35 mL of 0.11 M $Ni(NO_3)_2.6H_2O$ (99%, Smart Lab) stirring them for 15 min to form a homogenous solution. Then, 0.185 g of ammonium fluoride (NH_4F, Merck) and 0.48 g of urea (CH_4N_2O, Merck) were added to the solution. The rGO/NF obtained from the previous stage was cut into three parts with a size of 1 cm × 2 cm each, which were then put into the solution. It was then transferred into a Teflon-lines autoclave (100 mL) to undergo a hydrothermal process at 160°C for 6 h. The result of $NiMoO_4$/rGO/NF is washed with DI water and ethanol and then dried at 60°C overnight.

2.1.3 Electrodeposition of $Ni(OH)_2$ on $NiMoO_4$/rGO/NF

Electrodeposition was applied to attach $Ni(OH)_2$ to $NiMoO_4$/rGO/NF. 4 mmol potassium chloride (KCl 99%, SAP chemicals) was added slowly into 50 ml DI water. $Ni(NO_3)_2.6H_2O$ (1.75 g) was alternately added into the solution, then was magnetically stirred for 10 min. The previously prepared $NiMoO_4$/rGO/NF was transferred into the solution, and then a potential of 5 V was applied for 120 s to deposit $Ni(OH)_2$ on $NiMoO_4$/rGO/NF. The resulting samples were cleaned with DI water and ethanol and then dried in a vacuum at 60°C.

2.2 Characterizations

X-ray diffraction (XRD, Cu$K\alpha$, $\lambda = 1.54056$ Å) is used to analyze the obtained phase of each synthesis stage. The phase analysis was performed using Match! software. The functional groups, surface morphologies, and elemental compositions of samples were examined using Fourier transform infrared (FTIR, Nicolet iS10), scanning electron microscopy (SEM, INSPECT S50), and energy dispersive X-ray (EDX), respectively. Electrochemical tests were conducted on a half-cell with three-electrode setup. The capacitive performances of the $Ni(OH)_2$/$NiMoO_4$/rGO/NF electrodes were evaluated by cyclic voltammetry (CV) within the potential range of 0 V to 0.7 V and scan rates of 5 mV·s^{-1}, 10 mV·s^{-1}, 25 mV·s^{-1}, 50 mV·s^{-1}, 75 mV·s^{-1}, and 100 mV·s^{-1}. The CV measurement was performed in a 2 M KOH electrolyte with graphite as a counter electrode and a saturated calomel electrode (SCE) as a reference. The specific capacitance (C_S), energy density (E), and power density (P) of electrodes were calculated using Equation (1) to Equation (3), respectively.

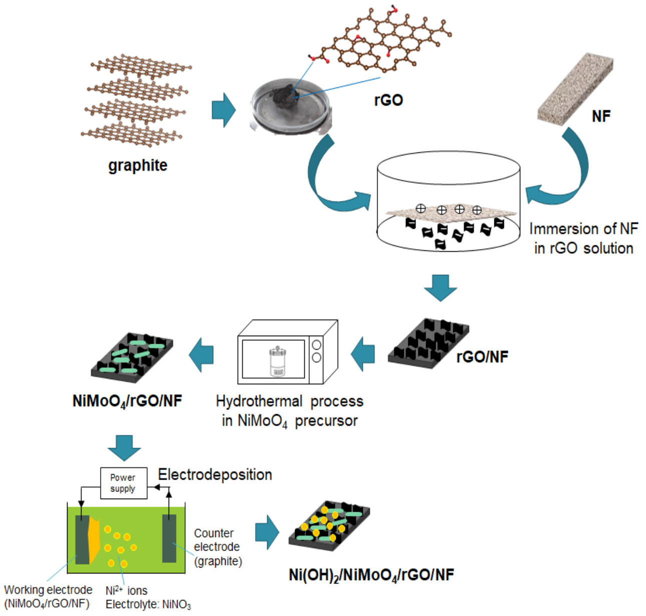

Figure 1. Schematic of the synthesis procedures of the $Ni(OH)_2$/$NiMoO_4$ on the rGO/NF electrode.

$$C_S = \frac{\int IdV}{2\Delta V\, mv}\ (\mathrm{F{\cdot}g^{-1}}) \quad (1)$$

$$E = \frac{\frac{1}{2}C_s(\Delta V)^2}{3.6}\ (\mathrm{Wh{\cdot}kg^{-1}}) \quad (2)$$

$$P = \frac{E \times 3600}{t}\ (\mathrm{W{\cdot}kg^{-1}}) \quad (3)$$

∫IdV represents the area within the I-V curve, ΔV describes the potential window, m is the mass of the electrode, v is the scan rate, and t is the discharge time. The m was determined from the mass difference between the sample and the bare NF. The conductivity of the electrodes was analyzed with Electrochemical Impedance Spectroscopy (EIS) within the frequency range of 102 Hz to 106 Hz. Lastly, the galvanostatic charge/discharge (GCD) tests evaluated charge-dicharge behaviors of the electrodes within the desired cycles. The discharged specific capacitance ($C_{\text{S-dis}}$) was calculated using Equation (4):

$$C_{\text{S-dis}} = \frac{{}^{I}\!/_{m} \times t}{\Delta V}\ (\mathrm{F{\cdot}g^{-1}}) \quad (4)$$

where I/m is the current density ($\mathrm{A{\cdot}g^{-1}}$), t is the discharge time, and ΔV is the potential window. The CV, EIS, and GCD measurements were performed using the same device (CS350 Potentiostat, Corrtest).

3. Results and discussion

3.1 Structural analysis

Figure 2(a) shows an illustration of the electrode evolution over the synthesis stages. The NF color changes to black when it is coated with rGO. A light green color is observed as $NiMoO_4$ is hydrothermally coated onto rGO/NF. The electrodeposition of $Ni(OH)_2$ on $NiMoO_4$/rGO/NF within the area of 1 cm × 1 cm results in a darker green color.

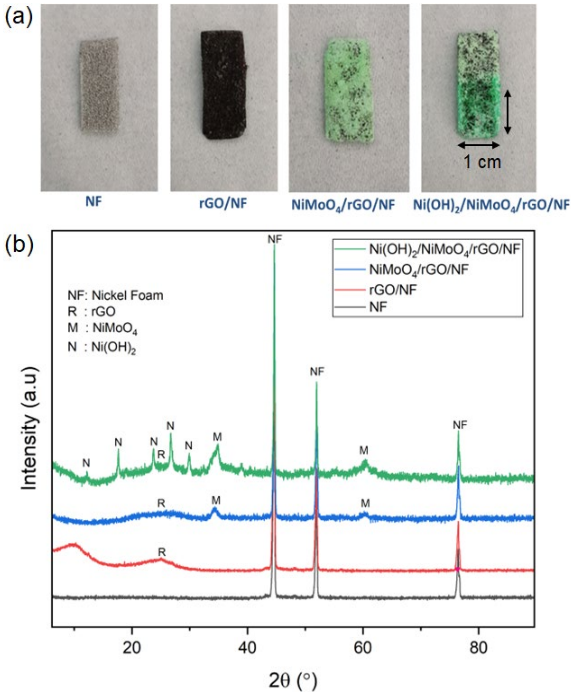

Figure 2. (a) Visualization, and (b) XRD patterns of the electrode over the synthesis steps.

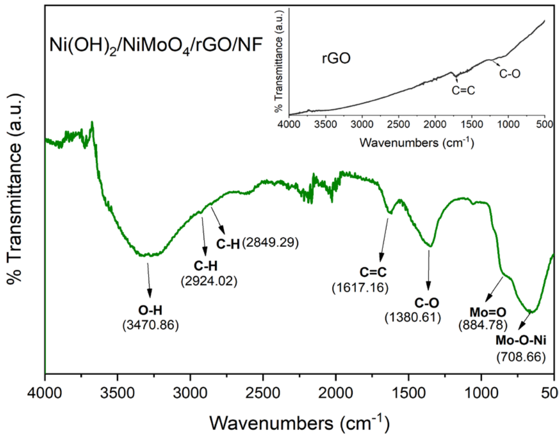

Figure 3. FTIR spectrum of the $Ni(OH)_2/NiMoO_4$/rGO/NF electrode. Inset is the spectrum of rGO.

XRD patterns of the electrode over the synthesis procedures are shown in Figure 2(b). NF shows sharp peaks at ~44.5°, ~51.8°, and ~76.4°, consistent with JCPDS card no. 04–0850 [19], which are dominant and remain over the procedures. A broad peak, typical of rGO, is observed at 2θ of ~24° to ~27°. Two additional peaks at ~33.9° and ~60.2° corresponding to $NiMoO_4$ (JCPDS card no. 45-0142) are seen in $NiMoO_4$/rGO/NF, which is consistent with that reported in [20]. The presence of $Ni(OH)_2$ is confirmed by XRD peaks at ~12.1°, 18.8°, 23.6°, 27.1°, 29.6°, 32.1°, 34.6°, and 54.8° (JCPDS card no. 38-0715) as described by Zhang *et al.* [12]. This result confirms that the electrodeposition process successfully yields $Ni(OH)_2/NiMoO_4$ composites on the rGO/NF template.

The functional groups present in the $Ni(OH)_2/NiMoO_4$/rGO/NF electrode were evaluated from the FTIR spectrum, as displayed in Figure 3. The electrode has functional groups of Mo–O–Ni at 708.66 cm^{-1} and Mo=O at 884.78 cm^{-1}, which indicates $NiMoO_4$ [21]. C–O and C=C as characteristic bonds of rGO are observed at 1380.61 cm^{-1} and 1617.16 cm^{-1}, respectively. This is in accordance with the FTIR spectrum of pristine rGO as shown in the inset of Figure 3. Moreover, the asymmetric C–H at 2924.02 cm^{-1}, symmetric C–H at 2849.29 cm^{-1}, and O–H at 3470.86 cm^{-1} are indications of the presence of $Ni(OH)_2$ in the $Ni(OH)_2/NiMoO_4$ composite [22]. While the FTIR analysis was focused on the final composite to confirm the coexistence of $Ni(OH)_2$, $NiMoO_4$, and rGO functional groups, the spectra of the resulting sample in each stage were not included here, as their structural identities were verified by XRD and SEM/EDX analyses.

The surface morphologies of rGO and $Ni(OH)_2/NiMoO_4$/rGO/NF are presented in Figure 4(a-b), respectively. rGO shows wrinkle stacking layers having some parts that are more transparent and thinner compared with others, which confirms the existence of multi-layer rGO. This is a typical rGO structure obtained from both graphite [18] and biomass [7,23]. The thin layer-like nature of rGO remains in the $Ni(OH)_2$/ $NiMoO_4$/rGO/NF electrode, and it is visible on a surface that appears more indented. Urchin-like and nanosphere-like particles were also observed, and they spread all over the surface. It has been previously reported that $NiMoO_4$ has a structure resembling that of sea urchins [24], while $Ni(OH)_2$ looks like a nano-sized sphere [12]. The SEM image hence verifies the presence of the $Ni(OH)_2/NiMoO_4$ composite on the rGO/NF template, which is consistent with the XRD data.

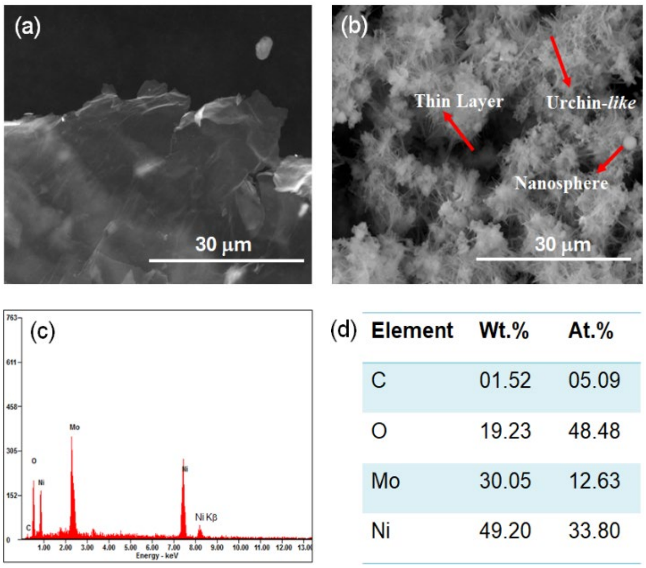

Element	Wt.%	At.%
C	01.52	05.09
O	19.23	48.48
Mo	30.05	12.63
Ni	49.20	33.80

Figure 4. SEM images of (a) rGO and (b) the $Ni(OH)_2/NiMoO_4$/rGO/NF electrode, (c) its EDX spectrum, and (d) the relative weight (wt%) and atomic (at%) percentages of the observed K emission of each element.

The EDX spectrum of the $Ni(OH)_2/NiMoO_4$/rGO/NF electrode is presented in Figure 4(c), showing the presence of Ni, Mo, C, and O peaks. Three characteristic Ni emissions are identified: (i) Ni-L at ~1 keV, (ii) Ni-Kα at ~7.5 keV, and (iii) Ni-Kβ at ~8.2 keV. Similar Ni emissions have also been reported in previous studies [25,26]. The relative weight (wt%) and atomic (at%) percentages of each element, calculated from the K emissions, are summarized in Figure 4(d). Ni, Mo, and O are relatively dominant, consistent with their presence in the $Ni(OH)_2/NiMoO_4$ composite on the surface of the electrode.

3.2 Electrochemical properties

Figure 5(a) displays the current-potential (I-V) curves of the NF, rGO/NF, $NiMoO_4$/rGO/NF, and $Ni(OH)_2/NiMoO_4$/rGO/NF electrodes obtained from each synthesis step at a scan rate of 5 $mV\cdot s^{-1}$. The bare NF exhibited a relatively low current response, indicating limited electrochemical activities with relatively small charge storage [19]. However, a closed view of the curve shows a small redox peak at 0.2 V to 0.3 V, which can be associated with the electrochemical behavior of Ni in the KOH electrolyte. When Ni is oxidized in the electrolyte, it forms $Ni(OH)_2$ or NiO(OH), while during reduction, NiO(OH) is reduced back to $Ni(OH)_2$ [14]; thus, the redox process is reversible. This behavior, along with its high surface area, makes NF a robust electrode template for rechargeable battery systems. When NF is coated with rGO, the current is slightly enhanced, showing that rGO provides better conductivity but does not significantly contribute to the redox activity.

A noticeable increase in current was observed when $NiMoO_4$ was deposited on the rGO/NF substrate. The redox peak became more prominent, which is likely due to the catalytic activity of $NiMoO_4$. In addition to its good structural and thermal stability, $NiMoO_4$ exhibits multiple reversible redox reactions associated with Ni^{2+}/Ni^{3+} and Mo^{6+}/Mo^{5+}, which contribute to additional redox-active sites and enhance the overall charge storage capacity [27]. The $Ni(OH)_2/NiMoO_4$/rGO/NF showed the highest current response, indicating a significant enhancement of the redox reactions, likely involving $Ni(OH)_2$/NiOOH and $NiMoO_4$, as indicated in Equation (5) and Equation (6) [28,29].

$$Ni(OH)_2 + OH^- \leftrightarrow NiOOH + H_2O + e^- \qquad (5)$$

$$NiMoO_4 + OH^- \leftrightarrow NiOOH + MoO_4^{2-} + H_2O + e^- \qquad (6)$$

The largest I-V curve area also confirms that this electrode exhibits the highest specific capacitance at 5 $mV\cdot s^{-1}$ compared to the others. Moreover, all curves display typical pseudocapacitive behavior rather than electric double-layer capacitor (EDLC) [30]. The incorporation of $Ni(OH)_2$ onto $NiMoO_4$/rGO/NF creates a synergistic effect, providing more accessible active sites, enhancing electron transport through rGO, and improving stability and ionic diffusion due to the hierarchical structure of the electrode. All electrodes show a continuous and rapid increase in current without a distinct peak as the potential exceeds ~0.5 V. This increase is characteristic of non-Faradaic or pseudocapacitive behavior, in which redox reactions occur rapidly at or near the surface [30]. Another possibility is that water oxidation to oxygen (OER) [31] begins to dominate at ~0.5 V. Therefore, the observed current increase may result from a combination of pseudocapacitive behavior and the onset of OER.

The I-V curves of the $Ni(OH)_2/NiMoO_4$/rGO/NF electrode at various scan rates are shown in Figure 5(b). Redox peaks are prominent at low scan rate but become less noticable as the scan rate increases. The C_S, E, and P values of each electrode at varying scan rate were estimated by applying Equation (1) to Equation (3), and the results are plotted in Figure 5(c). All exhibit a decreasing trend in the C_S value as the scan rate increases. At the 5 $mV\cdot s^{-1}$ scan rate, the C_S is higher because ions have sufficient time to access the electrode surface and pores, while a decrease in the C_S as the scan rate increases is due to limited ion diffusion at higher rates [14,32]. It is clearly shown that $Ni(OH)_2/NiMoO_4$/rGO/NF has the highest C_S at low scan rate, but it drops the most. By comparing to the initial C_S at 5 $mV\cdot s^{-1}$, it has ~21% retention at 100 $mV\cdot s^{-1}$. On the other hand, rGO/NF maintained better retention at high scan rates, although it had the lowest C_S at low scan rates. rGO/NF is more like surface-based storage (EDLC behavior), while in $Ni(OH)_2/NiMoO_4$/rGO/NF, ion diffusion at high scan rates is limited because of the slower kinetics of redox processes and that ions can not access deeper redox sites effectively [14]. The Ragone plot in the inset of Figure 5(c) emphasizes that $Ni(OH)_2/NiMoO_4$/rGO/NF has the highest energy density and maintains good power density, making it suitable for high-performance energy storage applications.

Figure 5(d) presents the Nyquist plot of electrodes. The data is fitted using an equivalent circuit consisting of R_S, R_{CT}, CPE, and Z_W, which represent the solution resistance, charge transfer resistance, constant phase element, and Warburg impedance, respectively. The Z_W is associated with the straight line at low frequency and is related to ion diffusion [32]. Among the presented plots, $Ni(OH)_2/NiMoO_4$/rGO/NF has the smallest semicircle at high frequencies, indicating the lowest R_{ct}, and a steeper slope, implying better capacitance. At the constant frequency of 0.01 kHz, the electrical conductivity was enhanced in the order of NF (0.35 $S\cdot m^{-1}$), rGO/NF (0.92 $S\cdot m^{-1}$), $NiMoO_4$/rGO/NF (1.07 $S\cdot m^{-1}$), and $Ni(OH)_2/NiMoO_4$/rGO/NF (1.30 $S\cdot m^{-1}$).

The GCD curves of $Ni(OH)_2/NiMoO_4$/rGO/NF at various scan rates (Figure 5(e)) exhibit quasi-triangular shapes with slight deviations from linearity, indicating a combination of EDLC and pseudocapacitance contributions. As the current density increases, the discharge time decreases significantly, reflecting the limited ion diffusion and shorter interaction time with active sites at higher rates. The longest discharge duration at 0.25 A·g^{-1} demonstrates the highest $C_{\text{S-dis}}$ under low-rate conditions, whereas higher current densities yield lower $C_{\text{S-dis}}$ but better rate capability, confirming the electrode's suitability for high-power applications.

The GCD responses of the electrode at of 0.25 A·g^{-1} are shown in Figure 5(f). The non-linear (pseudocapacitive) profile becomes more pronounced in NiMoO$_4$/rGO/NF and Ni(OH)$_2$/NiMoO$_4$/rGO/NF, indicating a contribution from Faradaic redox processes. Among the samples, Ni(OH)$_2$/NiMoO$_4$/rGO/NF exhibits the longest discharge time, reflecting its highest specific capacitance and superior energy storage capability. The nearly triangular shapes of the curves suggest good electrochemical reversibility and minimal internal resistance [32]. The inset is the $C_{\text{S-dis}}$ values of Ni(OH)$_2$/NiMoO$_4$/rGO/NF at 0.25 A·g^{-1} over 50 cycles, demonstrating a retention rate of ~86%, indicative of fairly stable cycling performance.

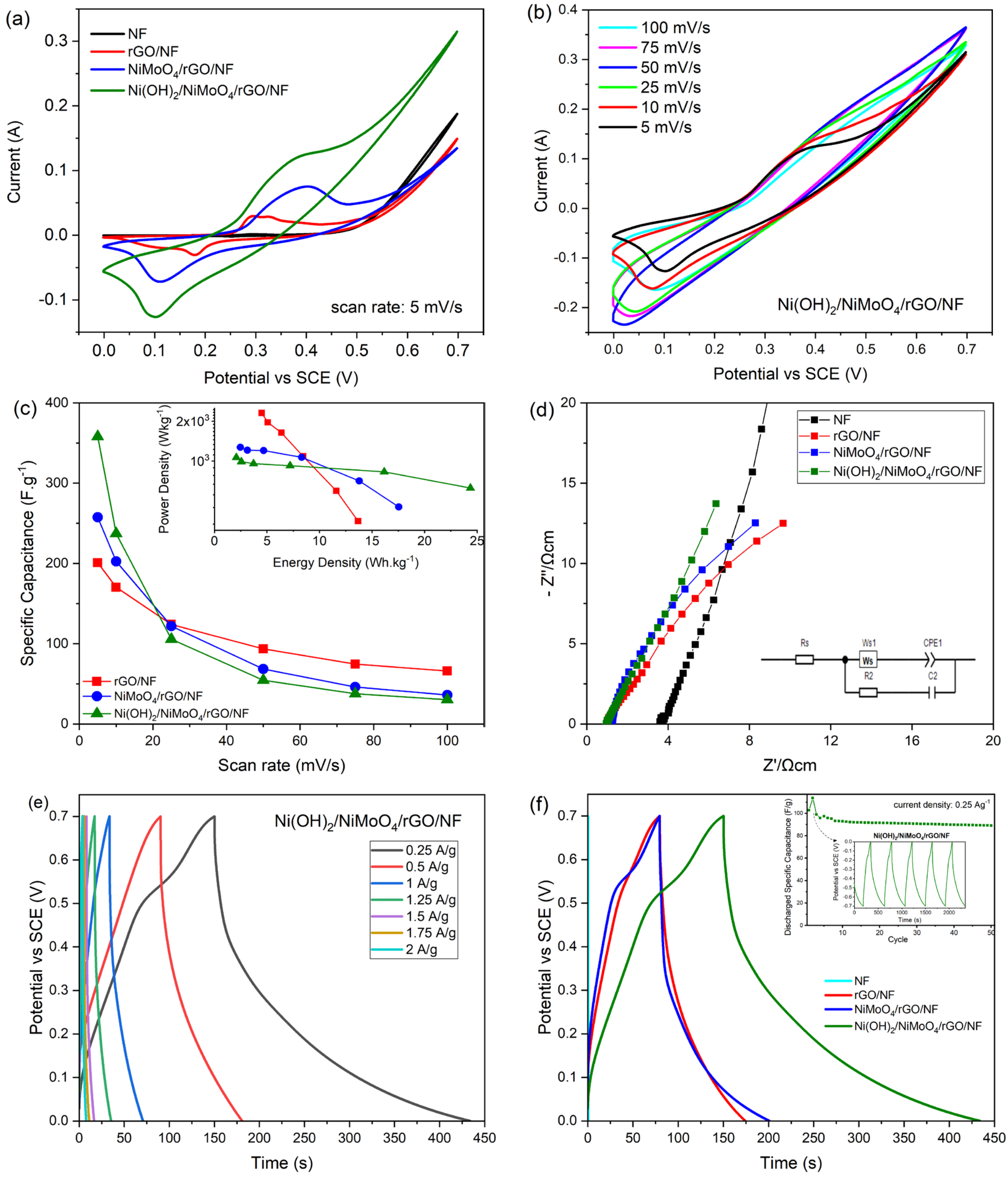

Figure 5. (a) I-V curves of NF, rGO/NF, NiMoO$_4$/rGO/NF, and Ni(OH)$_2$/NiMoO$_4$/rGO/NF electrodes at 5 mV·s^{-1}, (b) I-V curves of Ni(OH)$_2$/NiMoO$_4$/rGO/NF at various scan rates, (c) The C_S vs. scan rate for all electrodes; inset is power density vs. energy density, (d) Nyquist plots with the equivalent circuit, (e) GCD curves of Ni(OH)$_2$/NiMoO$_4$/rGO/NF at various current densities, and (f) GCD curves of the electrodes at 0.25 A·g^{-1}. Inset is the discharged C_S over 50 cycles with 86% retention.

Table 1. Comparison of Cs values measured in a three-electrode setup of this study with previous reports.

Material composition	**Preparation method**	**Electrolyte**	**Current density/ scan rate**	**Specific capacitance**	**Ref.**
$Ni(OH)_2/NiMoO_4$ on rGO-coated NF	Hydrothermal and electrodeposition	2 M KOH	5 $mV\cdot s^{-1}$	358 $F\cdot g^{-1}$	This study
$Ni(OH)_2$/rGO nanorods on NF	Hydrothermal	6 M KOH	1 $A\cdot g^{-1}$	1143 $F\cdot g^{-1}$	[33]
$Ni(OH)_2/g\text{-}C_3N_4$/rGO on NF	Hydrothermal	6 M KOH	1 $A\cdot g^{-1}$	543.8 $F\cdot g^{-1}$	[34]
$NiMoO_4$ on NF	Hydrothermal	3 M KOH	7 $A\cdot g^{-1}$	1740 $F\cdot g^{-1}$	[35]
$NiMoO_4@Ni(OH)_2$ on NF	Hydrothermal and electrodeposition	2 M KOH	4 $mA\cdot cm^{-2}$	7.43 $F\cdot cm^{-2}$	[36]
$Ni(OH)_2@CoMoO_4$ on NF	Hydrothermal and electrodeposition	2 M NaOH	8 $mA\cdot cm^{-2}$	5.23 $F\cdot cm^{-2}$	[37]
$NiMoO_4/WO_3$ on NF	Hydrothermal	3 M KOH	1 $A\cdot g^{-1}$	429.46 $F\cdot g^{-1}$	[38]
$Mo_4V_6O_{25}$ on Ni foil	Wet chemical	1 M KOH	1 $A\cdot g^{-1}$	203 $C\cdot g^{-1}$	[39]
$Ag_2Mo_2O_7$ on Ni foil	Wet chemical	1 M KOH	1 $A\cdot g^{-1}$	430 $C\cdot g^{-1}$	[40]
$ZrMo_2O_8$ on Ni foil	Wet chemical	1 M KOH	1 $A\cdot g^{-1}$	288 $C\cdot g^{-1}$	[41]
$SrMoO_4$ on Ni foil	Wet chemical	1 M KOH	5 $mV\cdot s^{-1}$	384 $C\cdot g^{-1}$	[42]

A summary of the electrochemical performance of this work compared with prior related materials is presented in Table 1. The comparison includes electrolyte type, current density or scan rate, preparation method, and electrode configuration. Although our specific capacitance is lower than that of some high-performing systems, this study provides valuable proof-of-concept evidence for the integration of $Ni(OH)_2/NiMoO_4$ composites with rGO on NF, highlighting a balanced approach to enhancing energy density, conductivity, and cycling stability. This hybrid electrode design provides a promising foundation for future optimization toward high-performance supercapacitor applications.

4. Conclusions

In this study, a hierarchical $Ni(OH)_2/NiMoO_4$ composite was successfully synthesized on an rGO-coated NF (rGO/NF) template through a combination of hydrothermal growth and electrodeposition. Structural analyses confirmed the integration of $Ni(OH)_2$ nanospheres and $NiMoO_4$ urchin-like structures on rGO/NF, providing abundant redox-active sites and enhanced electrical conductivity. Electrochemical evaluation demonstrated that the $Ni(OH)_2/NiMoO_4$/rGO/NF electrode achieved a high specific capacitance of ~358 $F\cdot g^{-1}$ at 5 $mV\cdot s^{-1}$, an energy density of ~24 $Wh\cdot kg^{-1}$, a power density of ~626 $W\cdot kg^{-1}$, and conductivity of 1.30 $S\cdot m^{-1}$ at 0.01 kHz. The electrode also retained ~86% of its capacitance after 50 charge-discharge cycles, indicating fair cycling stability. These results highlight the synergistic contribution of NF's structural support, rGO's conductivity, and the pseudocapacitive activity of $Ni(OH)_2/NiMoO_4$, making this hybrid architecture a promising candidate for next-generation high-performance hybrid battery-supercapacitor devices. For future studies, long-term cycling stability over higher cycle numbers and electrochemical measurements in a two-electrode (coin cell) configuration should be conducted to further assess the electrode's durability and practical applicability.

Acknowledgements

This work was supported by JSPS Core-to-Core Program (grant number: JPJSCCB20240005) and ITS Research Grant No. 1109/PKS/ITS/2024.

References

[1] "Home | Statistical Review of World Energy." Accessed: Dec. 10, 2024. [Online]. Available: https://www.energyinst.org/statistical-review

[2] J. L. Holechek, H. M. E. Geli, M. N. Sawalhah, and R. Valdez, "A global assessment: can renewable energy replace fossil fuels by 2050?," *Sustainability*, vol. 14, no. 8, p. 4792, 2022.

[3] S. Najib, and E. Erdem, "Current progress achieved in novel materials for supercapacitor electrodes: mini review," *Nanoscale Advances*, vol. 1, no. 8, pp. 2817–2827, 2019.

[4] F. Naseri, S. Karimi, E. Farjah, and E. Schaltz, "Supercapacitor management system: A comprehensive review of modeling, estimation, balancing, and protection techniques," *Renewable and Sustainable Energy Reviews*, vol. 155, p. 111913, 2022.

[5] H. Li, H. Xuan, J, Gao, T. Liang, X. Han, Y. Guan, J. Yang, P. Han, and Y. Du, "Construction of core-shell cobalt sulfide/manganese molybdate nanostructure on reduced graphene oxide/Ni foam as an advanced electrode for high-performance asymmetric supercapacitor," *Electrochimica Acta*, vol. 312, pp. 213–223, 2019.

[6] E. T. Mombeshora, and E. Muchuweni, "Dynamics of reduced graphene oxide: Synthesis and structural models," *RSC Advances*, vol. 13, no. 26, pp. 17633–17655, 2023.

[7] R. Asih, H. Nurdiansah, M. Zainuri, D. S. Khaerudini, A. T. Setiawan, A. Y. Dias, P. Untoro, A. Sholih, and Darminto, "Simple and high-yield synthesis of a thinner layer of graphenic carbon from coconut shells," *Journal of Renewable Materials*, vol. 12, no. 5, pp. 969–979, 2024.

[8] S. Stankovich, D. A. Dikin, R. D. Piner, K. A. Kohlhaas, A. Kleinhammes, Y. Jia, Y. Wu, S. T. Nguyen, and R. S. Ruoff, "Synthesis of graphene-based nanosheets via chemical reduction of exfoliated graphite oxide," *Carbon N Y*, vol. 45, no. 7, pp. 1558–1565, 2007.

[9] A. T. Smith, A. M. LaChance, S. Zeng, B. Liu, and L. Sun, "Synthesis, properties, and applications of graphene oxide/reduced graphene oxide and their nanocomposites," *Nano Materials Science*, vol. 1, no. 1, 2019.

[10] P. K. Sahoo, N. Kumar, A. Jena, S. Mishra, C.-P. Lee, S-Y. Lee, and S-J. Park, "Recent progress in graphene and its derived hybrid materials for high-performance supercapacitor electrode applications," *RSC Advances*, vol. 14, no. 2, pp. 1284–1303, 2024.

[11] P. Kantichaimongkol, T. Wanotayan, and J. Qin, "Review on surface engineering of NMC for high performance of lithium-ion batteries," *Journal of Metals, Materials and Minerals*, vol. 35, no. 2, p. e2338, 2025.

[12] R. Zhang, Q. Tu, X. Li, X. Sun, X. Liu, and L. Chen, "Template-free preparation of α-Ni(OH)$_2$ nanosphere as high-performance electrode material for advanced supercapacitor," *Nanomaterials*, vol. 12, no. 13, p. 2216, 2022.

[13] J. Li, X. Chang, X. Zhou, and M. Zhang, "Design of Ni(OH)$_2$ nanosheets@NiMoO$_4$ nanofibers' hierarchical structure for asymmetric supercapacitors," *Nanomaterials*, vol. 12, no. 22, p. 4079, 2022.

[14] X. Zhang, and Y. Xu, "The fabrication of hierarchical NiMoO$_4$ @Ni(OH)$_2$ nanocomposites and its electrochemical behavior used as supercapacitor electrode," *Inorganic Chemistry Communications*, vol. 87, pp. 8–11, 2018.

[15] Y. Zhang, C.-r. Chang, H.-l. Gao, S.-w. Wang, J. Yan, K.-z. Gao, X.-d. Jia, H.w. Luo, H. Fang, A.-q. Zhang, and L-z. Wang, "High-performance supercapacitor electrodes based on NiMoO$_4$ nanorods," *Jounal of Materials Research,* vol. 34, no. 14, pp. 2435–2444, 2019.

[16] T. Mawintorn, K. Lolupiman, N. Kiatwisarnkij, P. Woottapanit, M. Karnan, S. S. Na Ayuttaya, X. Zhang, P. Wangyao, and J. Qin, "Fabrication and characterization of zinc anode on nickel conductive cloth for high-performance zinc ion battery applications," *Journal of Metals, Materials and Minerals*, vol. 34, no. 3, p. e2083, 2024.

[17] X. Ling, F. Du, Y. Zhang, Y. Shen, T. Li, A. Alsaedi, T. Hayat, Y. Zhou, and Z. Zou, "Preparation of an Fe$_2$Ni MOF on nickel foam as an efficient and stable electrocatalyst for the oxygen evolution reaction," *RSC Advances*, vol. 9, no. 57, pp. 33558–33562, 2019.

[18] D. C. Marcano, D. Kosynkin, J. M. Berlin, A. Sinitskii, Z. Sun, A. Slesarev, L. B. Alemany, W. Lu, and J. Tour, "Improved synthesis of graphene oxide," *ACS Nano*, vol. 4, no. 8, pp. 4806–4814, 2010.

[19] Y. Xu, H. Xuan, J. Gao, T. Liang, X. Han, J. Yang, Y. Zhang, H. Li, P. Han, and Y. Du, "Hierarchical three-dimensional NiMoO$_4$-anchored rGO/Ni foam as advanced electrode material with improved supercapacitor performance," *Journal of Materials Science*, vol. 53, no. 11, pp. 8483–8498, 2018.

[20] M. Yao, Z. Hu, Y. Liu, and P. Liu, "A novel synthesis of size-controllable mesoporous NiMoO$_4$ nanospheres for supercapacitor applications," *Ionics*, vol. 22, no. 5, pp. 1–9, 2016.

[21] A. P. De Moura, L. H. Oliveira, I. L. V. Rosa, C. S. Xavier, P. Lisboa-Filho, M. S. Li, F. L. Porta, E. Longo, and J. A. Varela, "Structural, optical, and magnetic properties of NiMoO nanorods prepared by microwave sintering," *Scientific World Journal*, vol. 2015, no. 1, p. 315084, 2015.

[22] E. G. C. Neiva, M. M. Oliveira, M. F. Bergamini, L. H. Marcolino, and A. J. G. Zarbin, "One material, multiple functions: Graphene/Ni(OH)$_2$ thin films applied in batteries, electrochromism and sensors," *Scientific Reports*, vol. 6, p. 33806, 2016.

[23] D. Ristiani, R. Asih, F. Astuti, M. Baqiya, C. Kaewhan, S. Tunmee, H. Nakajima, S. Soontaranon, and D. Darminto, "Mesostructural study on graphenic-based carbon prepared from coconut shells by heat treatment and liquid exfoliation.," *Heliyon*, vol. 8, no. 3, p. e09032, 2022.

[24] M. Jiang, Z. Hu, Y. Wang, C. Xiang, Y. Zou, F. Xu, Q. Yang, J. Zhang, and L. Sun, "NiMoO$_4$ @Co$_3$S$_4$ nanorods with core-shell structure for efficient hydrogen evolution reactions in electrocatalysts," *Journal of Alloys and Compounds*, vol. 927, p. 166824, 2022.

[25] L. Yedra, C. N. S. Kumar, A. Pshenova, E. Lentzen, P. Philipp, T. Wirtz, and S. Eswara, "A correlative method to quantitatively image trace concentrations of elements by combined SIMS-EDX analysis," *Journal of Analytical Atomic Spectrometry*, vol. 36, no. 1, pp. 56–63, 2021.

[26] J. Zhang, W. Xiang, Y. Liu, M. Hu, and K. Zhao, "Synthesis of high-aspect-ratio nickel nanowires by dropping method," *Nanoscale Research Letters*, vol. 11, no. 1, pp. 1–5, 2016.

[27] S. Zhang, M. Cen, Q. Wang, X. Luo, W. Peng, Y. Li, F. Zhang, and X. Fan, "Complete reconstruction of NiMoO$_4$/NiFe LDH for enhanced oxygen evolution reaction," *Chemical Communications*, vol. 59, no. 23, pp. 3427–3430, 2023.

[28] W. H. Sun, and X. Zhang, "NiMoO$_4$–mediated fabrication of Ni-based electrocatalyst for efficient water splitting," *Renewable Energy*, vol. 241, p. 122312, 2025.

[29] Y. H. Chung, I. Jang, J.-H. Jang, H. S. Park, H. C. Ham, J. H. Jang, Y.-K. Lee, and S. J. Yoo, "Anomalous in situ activation of carbon-supported Ni$_2$P nanoparticles for oxygen evolving electrocatalysis in alkaline media," *Scientific Report*, vol. 7, no. 1, pp. 1–8, 2017.

[30] S. Fleischmann, J. B. Mitchell, R. Wang, C. Zhan, D-en. Jiang, V. Presser, and V. Augustyn, "Pseudocapacitance: From fundamental understanding to high power energy storage materials," *Chemical Reviews*, vol. 120, no. 14, pp. 6738-6782, 2020.

[31] Y. Hao, X. Cao, C. Lei, Z. Chen, X. Yang, and M. Gong, "Chemical oxygen species on electrocatalytic materials during oxygen evolution reaction," *Materials Today Catalysis*, vol. 2, p. 100012, 2023.

[32] C. Sandford, M. A. Edwards, K. J. Klunder, D. P. Hickey, M. Li, K. Barman, M. S. Sigman, H. S. White, and S. D. Minteer, "A synthetic chemist's guide to electroanalytical tools for studying reaction mechanisms," *Chemical Science*, vol. 10, no. 26, pp. 6404–6422, 2019.

[33] L. Xu, H. Chen, and K. Shu, "Ni(OH)$_2$/RGO nanosheets constituted 3D structure for high-performance supercapacitors," *Journal of Sol-Gel Science and Technology*, vol. 77, no. 2, pp. 463–469, 2016.

[34] H. Liu, B. Liu, X. Sun, X. Han, J. Cui, Y. Zhang, and W. He, "A simple hydrothermal method for the preparation of 3D petal-like Ni(OH)$_2$/g-C$_3$N$_4$/RGO composite with good supercapacitor performance," *Inorganic Chemistry Communications,* vol. 122, p. 108263, 2020,

[35] Y. Zhang, H-l. Gao, X-d. Jia, S-w. Wang, J. Yan, H-w. Luo, K-z. Gao, H. Fang, A-q. Zhang, and L-z. Wang, "$NiMoO_4$ nanorods supported on nickel foam for high-performance supercapacitor electrode materials," *Journal of Renewable and Sustainable Energy*, vol. 10, no. 5, p. 054101, 2018.

[36] G. Jiang, M. Zhang, X. Li, and H. Gao, "$NiMoO_4$@$Ni(OH)_2$ core/shell nanorods supported on Ni foam for high-performance supercapacitors," *RSC Advances*, vol. 5, no. 85, pp. 69365–69370, 2015,

[37] X. Li, S. Y. Lin, M. Zhang, G. Jiang, and H. Gao, "Construction of hierarchical $Ni(OH)_2$@$CoMoO_4$ nanoflake composite for high-performance supercapacitors," *Nano*, vol. 11, no. 5, p. 1650050, 2016.

[38] I. K. Durga, D. K. Kulurumotlakatle, T. Ramachandran, Y. A. Kumar, D. A. Reddy, K. V. G. Raghavendra, A. A. Alothman, and S. S. Rao, "Synergy unleashed: $NiMoO_4/WO_3$/NF nanoflowers elevate for supercapacitor performance," *Journal of Physics and Chemistry of Solids*, vol. 186, p. 111811, 2024.

[39] S. Rajkumar, R. Prabakaran, S. Elaissi, and J. Princy Merlin, "Construction of nanostructured $Mo_4V_6O_{25}$ electrode material for high-performance asymmetric supercapacitors," *Journal of Inorganic and Organometallic Polymers and Materials*, pp. 1–10, 2025.

[40] R. Srinivasan, G. Krishnan, K. Mathivanan, S. Dhineshkumar, S. Ansar, P. Mohan, and J. P. Merlin, "One-step synthesis of nanostructured $Ag_2Mo_2O_7$ with enhanced efficiency for supercapacitors," *Ionics*, vol. 30, no. 11, pp. 7537–7549, 2024.

[41] S. Rajkumar, M. Karthikeyan, A. Manohar, S. Dhineshkumar, and J. Princy Merlin, "One-step synthesis and fabrication of $ZrMo_2O_8$ nanostructures as advanced electrode material for energy storage applications," *Journal of Industrial and Engineering Chemistry*, vol. 137, pp. 162–173, 2024.

[42] A. Sathiyan, S. Rajkumar, S. Dhineshkumar, and J. Princy Merlin, "Electrochemical performance of $SrMoO_4$ as electrode material for energy storage systems," *Journal of Industrial and Engineering Chemistry*, vol. 129, pp. 521–530, 2024.